

## Charge-Transfer-Induced Interfacial Exchange Coupling at the Co/BiFeO<sub>3</sub> Interface

Jianwei Meng<sup>1,2,3,†</sup>, Kai Chen<sup>2,4,5,†</sup>, Emin Mijit<sup>4</sup>, Dongfang Chen<sup>6</sup>, Fadi Choueikani<sup>4</sup>,  
Zhiqiang Zou<sup>3</sup>, Lingling Wang<sup>7</sup>, Gang Mu<sup>7</sup>, Wenping Geng<sup>8</sup>, Qingyu Kong<sup>4</sup>, Anquan Jiang<sup>6</sup>,  
Xi-Jing Ning<sup>1</sup> and Tsu-Chien Weng<sup>2,3,\*</sup>

<sup>1</sup>*Institute of modern physics, Fudan University, Shanghai 200433, China*

<sup>2</sup>*High Pressure for Science & Technology Advanced Research, Shanghai 201203, China*

<sup>3</sup>*School of Physical Science and Technology, ShanghaiTech University, Shanghai 201210, China*


<sup>4</sup>*SOLEIL, l'Orme des Merisiers, St. Aubin, BP48, 91192 Gif sur Yvette Cedex, France*

<sup>5</sup>*Helmholtz-Zentrum Berlin für Materialien und Energie, Albert-Einstein-Straße 15, 12489 Berlin, Germany*

<sup>6</sup>*State Key Laboratory of ASIC and system, School of Microelectronics, Fudan University, Shanghai 200433, China*

<sup>7</sup>*State Key Laboratory of Functional Materials for informatics, Shanghai Institute of Microsystem and information Technology, Chinese Academy of Sciences, Shanghai 200050, China*

<sup>8</sup>*Science and Technology on Electronic Test and Measurement Laboratory, North University of China, Taiyuan 030051, China*

 (Received 24 May 2019; revised manuscript received 29 July 2019; published 4 October 2019; corrected 5 January 2023)

The interplay between ferroelectricity and magnetism in multiferroic materials is of great scientific and technological interest, allowing magnetic control of ferroelectric properties and electric control of magnetic properties through the magnetoelectric coupling from interfacial strain, exchange bias, or charge-transfer process. We report the charge transfer at the Co/BiFeO<sub>3</sub> interface from which the interfacial exchange coupling is achieved with the formation of Fe<sup>2+</sup>. The x-ray linear dichroism and x-ray magnetic circular dichroism results reveal that the strain as well as the exchange coupling  $J_{ex}$  in BiFeO<sub>3</sub> (BFO) with periodic 109° domains are stronger than that in BFO with 71° domains, resulting in the higher coercive field of Co/BFO with 109° domain samples. The possible electric field control of the charge-transfer process at the Co/BFO interface enables an alternative class of electrically controllable magnetization, exchange bias, and giant magnetoresistive response of spintronic devices.

DOI: [10.1103/PhysRevApplied.12.044010](https://doi.org/10.1103/PhysRevApplied.12.044010)

### I. INTRODUCTION

The magnetoelectric coupling effect opens a wide array of alternative applications including spintronic devices, sensors, high density information storage devices, and other multiply controlled devices, which allow the reversal of the ferroelectric polarization by a magnetic field and/or the control of the magnetic order parameters by an electric field from the strain-induced magnetoelectric (ME) coupling and the charge-transfer process as well as the orbital reconstruction at the interface and the modulation of the exchange bias interaction [1–7]. Numerous investigations have been focused on the coupling between ferromagnetic (FM) and multiferroic materials such as La<sub>x</sub>Sr<sub>1-x</sub>MnO<sub>3</sub>/BFO, BFO/YBa<sub>2</sub>Cu<sub>3</sub>O<sub>7</sub>, and La<sub>0.5</sub>Ca<sub>0.5</sub>MnO<sub>3</sub>/BFO heterostructures because BFO is a

widely studied multiferroic perovskite with a ferroelectric Curie temperature of 1043 K and an antiferromagnetic Neel temperature of 643 K [8–11]. Through the manipulation of the ferroelectric state in BFO, the FM state can be controlled through exchange coupling at the interface between the BFO and the FM layer. With a rhombohedral structure, BFO has three possible domain patterns including 71°, 109°, and 180° types. Exchange enhancement or exchange bias has been observed in Co<sub>0.9</sub>Fe<sub>0.1</sub>/BFO heterostructures with stripelike (71°) or mosaiclike architectures (mixed with 71°, 109°, and 180°) ferroelectric domain walls [4,12] and the 109° or 180° domain walls have been suggested to be the possible source for the exchange bias [13–15]. Although many efforts have been made to investigate the interface coupling effect between BFO and other ferromagnetic materials, the coupling mechanism is not clearly understood and further investigations are required to understand the magnetic interaction at the FM/BFO interface.

\*wengzq@shanghaitech.edu.cn

†These authors contributed equally.

The interfacial structure and chemistry in those metal-metal oxide systems are crucial aspects to determine the ME coupling, and the oxidation of the metal is likely to take place, forming a complex metal-metal oxide interface [16]. Theoretically, Duan *et al.* predicted an interface magnetization due to the charge transfer from Fe to the interfacial Ti *d* band in the ideal TiO<sub>2</sub>-terminated Fe/BaTiO<sub>3</sub> structure [17], and the interface ferromagnetism of Fe/BaTiO<sub>3</sub> was later supported by the results of Valencia *et al.* by soft x-ray magnetic scattering investigations [18]. Electric control of magnetism has been achieved with the formation of FeO<sub>x</sub> at the Fe/BaTiO<sub>3</sub> interface [19,20]. A first-principles simulation suggests the charge transfer plays an important role in the emergence of ferromagnetism and the metallic electronic state at the BFO/YBa<sub>2</sub>Cu<sub>3</sub>O<sub>7</sub> interfaces [10]. BFO/La<sub>1-x</sub>Sr<sub>x</sub>MnO<sub>3</sub> has recently been proposed as a candidate to engineer three-dimensional topological insulators [21]. Induced interface ferromagnetism as well as exchange bias have been reported in La<sub>0.7</sub>Sr<sub>0.3</sub>MnO<sub>3</sub>/BFO [8,22–24] and in La<sub>0.5</sub>Ca<sub>0.5</sub>MnO<sub>3</sub>/BFO [11]; however, the charge-transfer process was only reported by Liang *et al.* from the Fe 2*p* core level x-ray photoemission spectra (XPS) at the manganite/BFO interface [25].

Demonstrating exchange bias coupling, BFO/Co<sub>0.4</sub>Fe<sub>0.4</sub>B<sub>0.2</sub> or BFO/Co<sub>0.9</sub>Fe<sub>0.1</sub> is suitable to accomplish 90° or 180° switching [26,27]. The magnetization of Co<sub>0.4</sub>Fe<sub>0.4</sub>B<sub>0.2</sub> or Co<sub>0.9</sub>Fe<sub>0.1</sub> can be manipulated by switching the electric polarization of BFO [28–32]. It is puzzling that the observed exchange bias of  $H_{EB} < 100$  Oe is roughly two orders smaller compared to the theoretical predicted value of  $H_{EB} = 6.5$  kOe [12]. In this work, the charge-transfer-induced interfacial exchange coupling at the Co/BFO interface is investigated to shed light on the exchange coupling mechanism at the metal/BFO interface. The observation of Fe<sup>2+</sup> at the interface reveals that the coupling between Co and BFO is achieved by the charge transportation. Our x-ray linear dichroism (XLD) and x-ray magnetic circular dichroism (XMCD) results indicate that the compressive strain in BFO with 109° domains is stronger than that in BFO with 71° domains, which is the reason that the magnetic coercive field is higher in the 109° domain samples. Our results confirming the charge-transfer-induced exchange coupling occurring at metal/BFO interfaces, in general, presents a clear picture of interface coupling, which is in favor of the application of alternative magnetoelectric coupling devices.

## II. EXPERIMENT

### A. Sample preparation

BFO thin films are fabricated on GdScO<sub>3</sub> (GSO) (110)<sub>o</sub> single crystal substrates by pulsed laser deposition method with a KrF excimer laser of  $\lambda = 248$  nm. The pulsed laser beam is focused on a Bi<sub>1.1</sub>FeO<sub>3</sub> ceramic target with an

energy density of approximately 2.5 J·cm<sup>-2</sup> and a repetition rate of 6 Hz. The spot size is fixed at 1.5 × 2.5 mm<sup>2</sup> by adjusting the defocus distance. In the process of film growth, the substrate temperature is set to 600 °C, which is confirmed by an infrared temperature instrument, and the oxygen pressure is stabilized at 10 Pa by adjusting the flow of oxygen. After the end of the deposition process, the temperature is kept constant for 10 min to form a smooth surface and then cooled to room temperature in the processing oxygen pressure.

The Co layer with a thickness of 4 nm is deposited by dc magnetron sputtering method at room temperature. Then the Ta layer with a thickness of 3 nm follows, which is a capping layer to prevent Co from being oxidized. The total thickness of the upper layers is about 7 nm, which is designed to weaken the signal of Fe<sup>3+</sup> from BiFeO<sub>3</sub> thin film. The base pressure is about 5 × 10<sup>-6</sup> Pa. During the process, the working gas (high purity Ar) is injected into the chamber to adjust the working pressure, which is needed to build up the glow. The power is set to 200 W, and finally, the deposition rate is fixed at 0.15 nm/s of Co and 0.18 nm/s of Ta.

### B. Piezo-force microscopy characterization

The surface topography and the domain structures of the BFO/GSO samples are measured by atomic force microscopy (Bruker Icon). Piezo-force microscopy (PFM) imaging of the samples is performed using a contact PtIr-coated silicon tip, and the tip bias is set to 7 V while the drive frequency is 25 kHz. In order to confirm the domain type, samples are rotated 90° to measure the in-plane (IP) and out-of-plane (OOP) images. The surface topography is measured using a tapping mode under ambient conditions to obtain a more distinct morphology. The tip radius used in the tapping mode (approximately 2 nm) is much smaller than that in the contact mode (approximately 20 nm).

### C. Magnetic hysteresis loops

The hysteresis loops are measured at temperatures ranging from 100 to 300 K by a vibrating sample magnetometer (Quantum Design's Magnetic Property Measurement System). Before the beginning of the measurement, the oscillating mode is set to eliminate any residual magnetic field. Then the samples are cooled to 4 K at the rate of 10 °C/min. Increasing the temperature to the testing point, the *M-H* measurement then begins. Because the GSO substrate is paramagnetic, the measurement result contains a large substrate contribution and small upper layer signals. In order to extract the ferromagnetic information in the upper layer, we separately measure the *M-H* data of the GSO substrates. Comparing and analyzing the data between the Co/BFO/GSO samples and the GSO

substrate, the magnetic hysteresis loops of the Co/BFO samples are finally obtained.

#### D. XAS, XLD, and XMCD measurements

X-ray absorption spectroscopy (XAS), XLD, and XMCD spectra at the Fe  $L_{2,3}$  and Co  $L_{2,3}$  edges, as well as the O  $K$  edge are measured at  $T=4$  K using a total electron yield mode (TEY) at Synchrotron-SOLEIL using the 7-T cryomagnet installed on the DEIMOS beamline. The XMCD studies are carried out using x-rays of circular right (CR) and left (CL) polarizations with a magnetic field of  $\mu_0 H = 6.5$  T applied along the x-ray beam, while the XLD is measured with linear polarized x-rays with a vertical (LV) or horizontal (LH)  $E$  vector. The XMCD and XLD data are recorded as  $(\sigma^+ - \sigma^-)$  and  $(\sigma^{LV} - \sigma^{LH})$ , respectively, where  $\sigma^+$  and  $\sigma^-$  denote the absorption cross sections for the right and left circular polarized x-rays and  $\sigma^{LV}$  and  $\sigma^{LH}$  denote the absorption cross sections for linear polarized x-rays with a vertical or horizontal  $E$  vector perpendicular to the propagation of the x-rays. With normal incidence [Fig. 3(e): left], the XLD spectra of  $(\sigma^a - \sigma^b)$  are obtained with the  $E$  vector of the x-ray parallel along the  $a$  or  $b$  axis, while with grazing incidence [Fig. 3(e): middle], the XLD spectra of  $(\sigma^{ab} - \sigma^c)$  are obtained with the  $E$  vector of the x-ray parallel along the  $a$ - $b$  plane or  $c$  axis.

### III. RESULTS AND DISCUSSION

#### A. AFM and PFM characterization

High quality epitaxial BFO thin films with  $71^\circ$  and  $109^\circ$  domains, called BFO71 and BFO109, respectively, are successfully prepared on the GSO (110)<sub>o</sub> substrates by the pulsed laser deposition method, and the parameters are carefully tuned to the process window [33,34]. The surface morphology and PFM images, including IP and OOP of the BFO thin films, are shown in Fig. 1. From Figs. 1(a) and 1(d), we can clearly see that the films grow with a step flow growth mode with a unit cell height no matter whether the samples have  $71^\circ$  or  $109^\circ$  stripelike domains, and the terrace width is about 150 nm. Figures 1(b) and 1(c) show the IP and OOP PFM images of the BFO109 samples. The stripelike domains are clearly shown in both IP and OOP images, which is consistent with the characteristics of  $109^\circ$  domains [35]. Interestingly, the step path is needle shaped and moves forward along the direction of the step in the BFO109 samples, with needle width of 55 nm. The stripe spacing indicates the period of the domain is about 59 nm, which is very close to the needle width. However, this value is as large as 280 nm in the  $71^\circ$  domain samples. For the BFO71 samples, OOP PFM images show obscured contrast as shown in Fig. 1(f), which suggests that all polarization variants are pointing

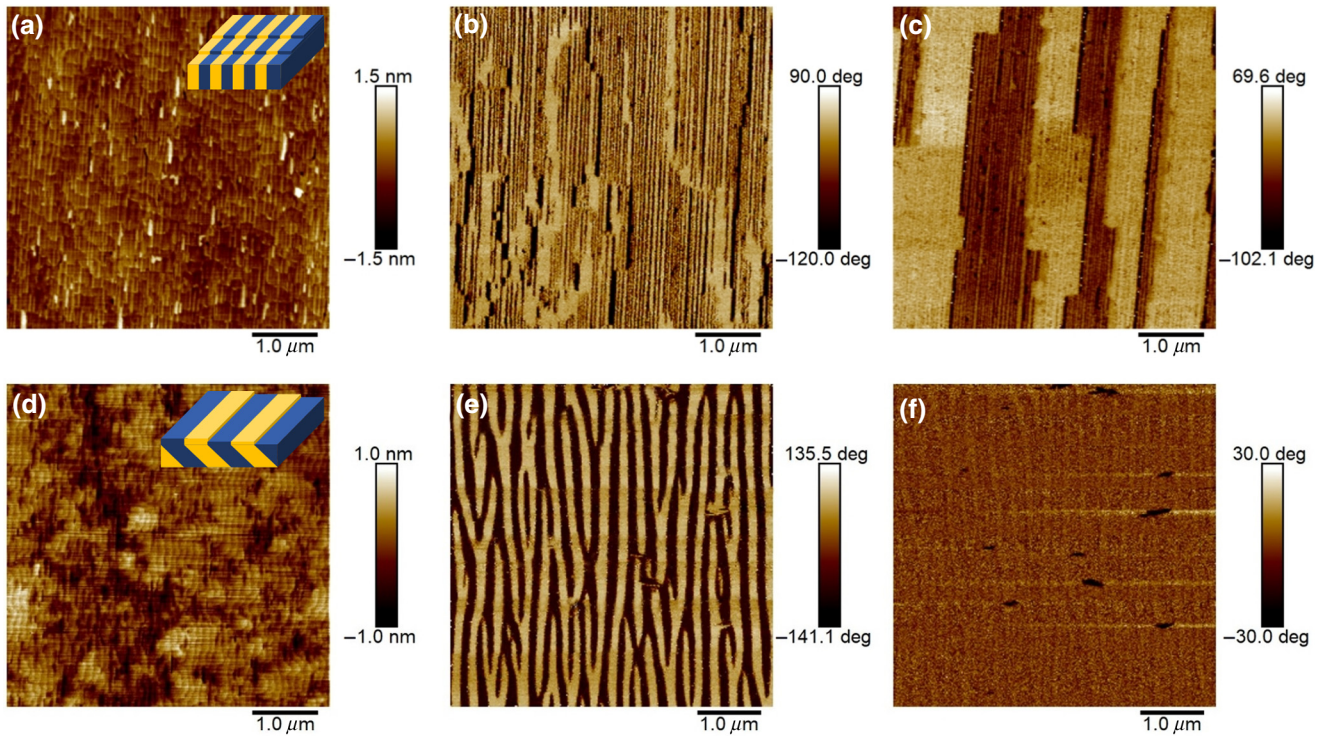


FIG. 1. The surface topography and PFM image of BiFeO<sub>3</sub> samples. (a) Topography, (b) in-plane PFM image, and (c) out-of-plane PFM image show the periodic  $109^\circ$  stripelike domain structure in BFO/GSO samples. (d) Topography, (e) in-plane PFM image and (f) out-of-plane PFM image indicate the  $71^\circ$  stripelike domain structure in BFO/GSO samples. The insets of (a),(d) show the relationship between the step advance and the domain styles of the BFO film.



downward toward the substrate, while the IP PFM images shown in Fig. 1(e) exhibit an obvious stripe image contrast essentially throughout the entire film. It is worth mentioning that the direction of the step forward is along the stripe domain in the BFO109 samples, while this direction is perpendicular to the stripe domain in the BFO71 samples, indicating the crucial role of the substrate induction in determining the final domain structure, which is consistent with the previous reports [15,33].

### B. Magnetic coupling at the Co/BFO interface

Ta/Co/BFO/GSO sandwich structures are fabricated to investigate the coupling effect of the two kinds of domains on the upper ferromagnetic layer. Macroscopic magnetic hysteresis loops are carried out using a vibrating sample magnetometer at  $T = 100, 150, 200, 250,$  and  $300$  K, and the applied field is along the  $[110]_O$  direction of the GSO substrates. Figure 2(a) shows typical magnetic hysteresis loops for the heterostructure of a single Co layer,  $\text{Fe}^{3+}$ , and Co/BFO109 samples at  $300$  K. A strong enhancement of the coercive field (40 Oe, blue curve) compared to that of the Co/GSO sample (18 Oe, black curve) is observed in Co/BFO109. While for Co/BFO71, only a weak enhancement of the coercive field (20 Oe, orange curve) is observed. The kinklike structure appearing near the coercive field or the splitting of the derivative magnetization peaks shown in Fig. 2(b) indicates the exchange coupling at the Co/BFO71 interface. The phenomenon of exchange coupling is usually observed in a ferromagnet-antiferromagnet (FM-AFM) bilayer, with a shifted hysteresis loop ( $H_{\text{EB}}$ ) or an enhanced coercivity ( $H_c$ ), or both [36]. In both heterostructures, only enhancement of the  $H_c$  is observed in the hysteresis without an exchange bias effect. If pinned or uncompensated spins at the BFO interface are

formed, which are not reversed by an external field, both the exchange bias and enhanced  $H_c$  will be observed in the hysteresis loop. Here, the absence of  $H_{\text{EB}}$  suggests that the spins at the BFO interface are not pinned and are rotatable with an external field.

The temperature dependence of the coercive field for the Co/BFO heterostructure [shown in Fig. 2(c)] clearly demonstrates the significant enhancement of the exchange coupling between the two layers at low temperatures, with the maximum coercive field reached at approximately 330 Oe in Co/BFO109 at 4 K, as derived from the XMCD intensity at the Co  $L_3$  edge (Supplemental Material [37]). With decreasing temperature, the  $H_c$  of all films (Co film,  $\text{Fe}^{3+}$ , and Co/BFO109) increases because of the enhancement of the Co film ferromagnetism and thus the coupling strengths. This enhancement is superimposed to the one associated with interfacial ferromagnetism. At the same temperature, assuming the same magnetization of the Co film and Co/BFO, the enhancement of the coercivity is from the interfacial magnetic coupling. At  $T = 100$  K, the  $H_c$  of Co/BFO/GSO is 150%–250% enhanced compared to that of Co on the bare GSO substrate.

### C. XLD and XMCD of BFO/GSO

A GSO single crystal has an orthorhombic structure with a lattice of  $a = 5.480$  Å,  $b = 5.746$  Å, and  $c = 7.932$  Å [38]. It is usually treated as a quasicubic (qc) structure and its  $(110)_o$  surface in the orthorhombic structure corresponds to the  $(100)_{\text{qc}}$  surface in the quasicubic structure. The equivalent lattice parameters are  $a_{\text{qc}} = c_{\text{qc}} = 3.970$  Å and  $b_{\text{qc}} = 3.966$  Å. The magnetic anisotropy of BFO grown on GSO is very sensitive to the lattice parameters, although there is only a very small difference between  $a_{\text{qc}}$  and  $b_{\text{qc}}$ . For the bulk BFO single crystal with a rhombohedral

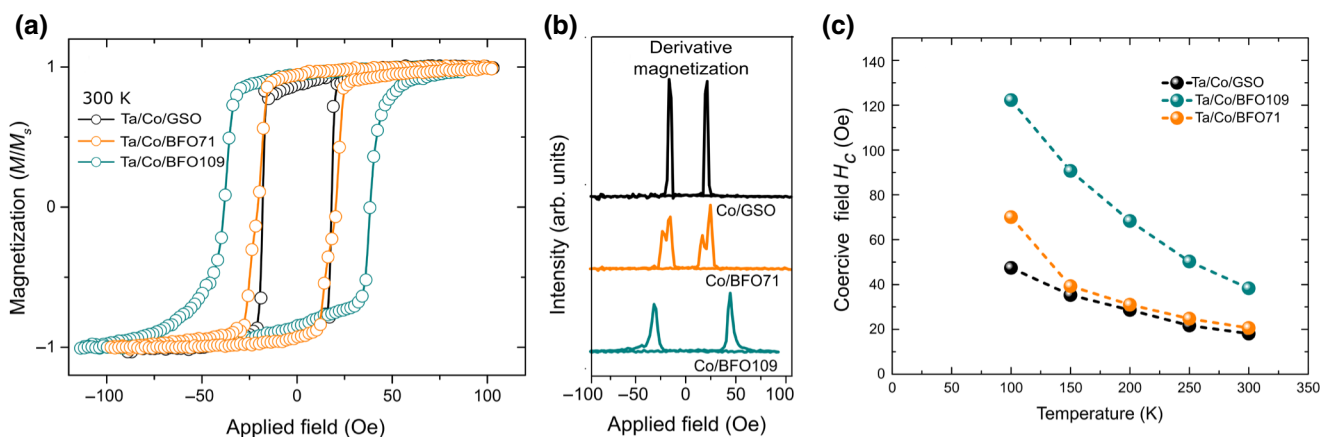


FIG. 2. Magnetic hysteresis of Co/BFO samples. (a) Room temperature magnetic hysteresis loops of a single Co layer (open black), Co/BFO71 (open orange), and Co/BFO109 (open blue) heterostructure measured with a magnetic field applied along the  $[100]$  direction. (b) The derivative of the magnetization curve of the samples. (c) Evolution of the coercive field  $H_c$  with temperature for samples Co (solid black), Co/BFO71 (solid orange), and Co/BFO109 (solid blue) as measured by Quantum Design's Magnetic Property Measurement System. Error bars are smaller than the points.

crystal structure, the ferroelectric polarization can be point along any  $\langle 111 \rangle$  direction. With consideration of the electrostatic and elastic boundary conditions, three possible periodic domain walls (i.e.,  $71^\circ$ ,  $109^\circ$ ,  $180^\circ$ ) are formed, which are distinguished by the angle polarization rotations across the domain wall [39,40]. Bulk BFO has a cycloidal spin structure and epitaxial BFO films exhibit four AFM axes, possessing a high spin  $\text{Fe}^{3+}$  ion with a  $2p^6 3d^5$  ground state.

Theoretical study has proposed that a weak FM moment can be induced in BFO films via the Dzyaloshinskii–Moriya (DM) interaction [41], and the weak ferromagnetism was later experimentally observed in a single-domain BFO film [42]. The coupling of the ferromagnetic moments of the Co to the canted moments of the BFO domain surface give rise to the exchange enhancement observed in both types of BFO films. The stronger enhancement observed in Co/BFO109 [Fig. 2(c)] suggests

an intriguing difference in the magnetic behavior of the two types of domain structures in BFO/GSO.

The polarization dependence with respect to the magnetization axis shows up as variations in the peak intensities, and the crystal field effect may also cause the shifts in the peak positions [43]. The latter contribution is neglected assuming a similar crystal field in BFO with different domain structures. Thus, the spin orientation in the BFO films can be simply determined from the XLD intensity over the  $\text{Fe-}L_{2,3}$  edges. The AFM axis may rotate from the  $c$  axis to the  $ab$  plane with tensile or compressive strain [26]. As shown in Fig. 3(f), BFO/SrTiO<sub>3</sub> (STO) with strong compressive strain ( $c/a \sim 1.03$ ) will have its AFM axis roughly in the  $ab$  plane, resulting in the hugely different spectra with linear polarized x-rays ( $E \parallel c$  and  $E \parallel ab$ ) and strong XLD intensity, as shown in Figs. 3(a) and 3(d), respectively. No XLD intensity will be observed when the AFM axis is along the  $\langle 111 \rangle$  direction, or  $54.7^\circ$  from the surface normal. The XLD will change its sign when the

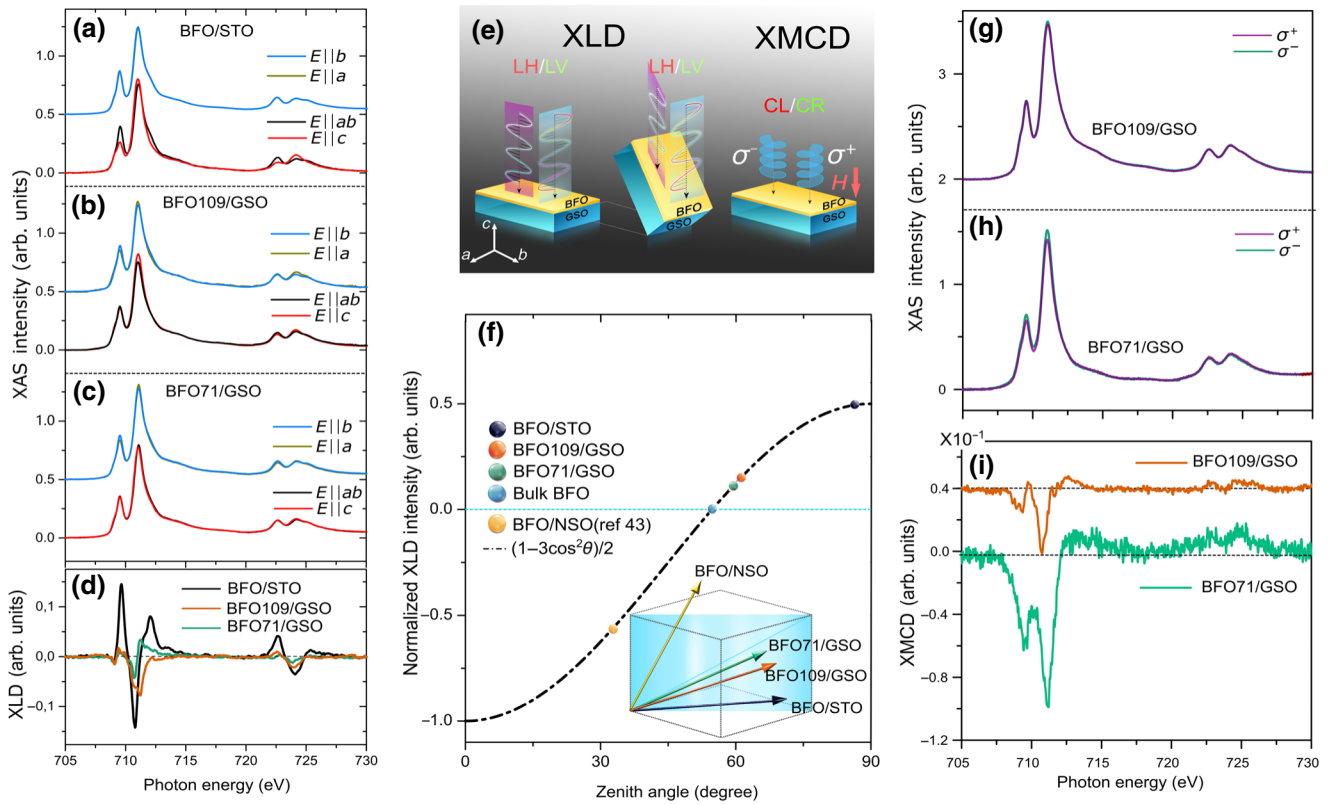


FIG. 3. X-ray absorption spectroscopy studies on  $\text{BiFeO}_3$  with  $71^\circ$  and  $109^\circ$  domains. Polarization-dependent  $\text{Fe}L_{2,3}$  spectra of BFO/STO (a), BFO/GSO thin films with  $109^\circ$  (b), and  $71^\circ$  (c) type domain with linear polarized x-rays, at  $T = 4$  K. The red and black curves correspond to the polarization of x-rays parallel to OOP and IP directions, respectively. (d) The corresponding XLD ( $\sigma^{ab} - \sigma^c$ ) with the intensity more reduced in BFO71/GSO. (e) A Schematic drawing of the experimental setup of XLD (left:  $E \parallel a$  and  $E \parallel b$ , middle:  $E \parallel ab$  and  $E \parallel c$ ) and XMCD (right), using linear or circular polarized x-rays, respectively. (f) The XLD intensity, controlled by the tensile or compressive strain in BFO, follows  $[1 - 3\cos^2\theta]/2$  with  $\theta$  the tilted angle of the mean AFM axis from the  $c$  axis. Polarization-dependent  $\text{Fe-}L_{2,3}$  spectra of BFO/GSO thin films with  $109^\circ$  (g) and  $71^\circ$  (h) type domains at 4 K with circular polarized x-rays parallel or antiparallel with the applied field  $\mu_0 H = 6.5$  T along the  $c$  axis, and the corresponding XMCD ( $\sigma^+ - \sigma^-$ ) spectra are shown in panel (i), which reveal much stronger dichroism in BFO films with  $71^\circ$  domain walls.

AFM axis is tilted from the surface normal with a small angle, as observed in BFO/NdScO<sub>3</sub> with the tensile strain [44]. For BFO/GSO with 71° and 109° domains, much weaker XLD are observed compared to that of BFO/STO due to the weaker compressive strain. The XLD intensity is proportional to  $[1-3\cos^2\theta]/2$  with  $\theta$  the tilted angle [Fig. 3(f)]. Thus, the AFM axes in BFO71 and BFO109 can be estimated to be approximately 59(5) and approximately 62(5) degrees tilted from the surface normal [Fig. 3(f)], with the strain slightly higher in BFO109. Our results indicate that the compressive strain in BFO with 109° domains is stronger than that in BFO with 71° domains. In addition, the difference between the  $E||a$  and  $E||b$  spectra is rather small, in accordance with the multi-AFM axis cycloidal along the [111] direction. It is worth mentioning that the direction of the magnetic moment is isotropic in the in-plane of the BFO (001)<sub>qc</sub> films [45]. The arrows shown in Fig. 3(f) only indicate the relative AFM axis of the magnetic moment Fe ions in BFO grown on various substrates.

DM interaction-induced canted moments in Co/BFO71 and Co/BFO109 is investigated with Fe  $L_{2,3}$  edge XAS [Figs. 3(g) and 3(h)] using circular polarized x-rays and the correspondence XMCD spectra [Fig. 3(i)], applying a magnetic field of 6.5 T along the surface normal. We observe a much stronger XMCD intensity in BFO71/GSO, which is 2.5 times higher than that of BFO109/GSO. This indicates the much weaker canted moments in BFO109/GSO, probably due to its much stronger AFM

exchange coupling  $J_{\text{ex}}$ . The XMCD intensity at the surface region of BFO71 is comparable to that observed at the BFO/La<sub>0.7</sub>Sr<sub>0.3</sub>MnO<sub>3</sub> interface, which is estimated to be approximately  $0.6 \mu_B/\text{Fe}$  atom, surprisingly larger than the canted moment ( $0.03 \mu_B/\text{Fe}$  atom) in the bulk BFO [8].

#### D. XMCD of Co/BFO/GSO with 71° and 109° domain walls

Ta/Co/BFO/GSO sandwich structures are fabricated to investigate the coupling effect of the two kinds of domains on the upper ferromagnetic layer. To address the mechanism of the magnetic coupling at the Co/BFO interface, XAS and XMCD spectra at Fe and the Co  $L_{2,3}$  edge are recorded together with the O  $K$  edge XAS and are shown in Fig. 4. As shown in Fig. 4(b), the Fe  $L_{2,3}$  edge XAS profile in Co/BFO/GSO, totally different from that of BFO/GSO with a typical Fe<sup>3+</sup> ( $3d^5$ ) [Fig. 4(a)] configuration, can be well reproduced with a high spin state Fe<sup>2+</sup> ( $3d^6$ ) configuration from atomic multiplet calculation using CTM4XAS [46] in an octahedral ( $O_h$ ) symmetry, convoluted with a Lorentzian function for lifetime broadening and a Gaussian to account for the instrumental resolution. The Slater integrals, which are scaled down to 80% of the atomic Hartree-Fock value with no reduction for the spin orbit coupling parameter of  $\zeta$ , are used for the calculation of Fe<sup>3+</sup> and Fe<sup>2+</sup> as shown in Figs. 4(a) and 4(b). Different values of 10 Dq of 2.0 and 1.2 eV are used for the multiplet

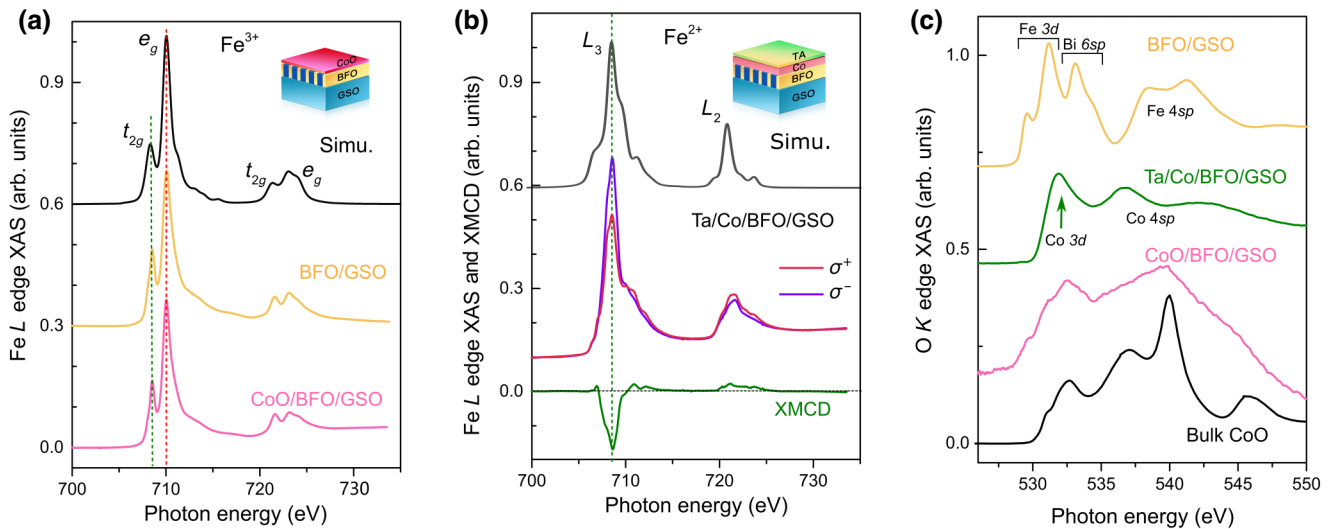


FIG. 4. X-ray absorption spectroscopy studies on Co/BFO with 71° and 109° domains. The Fe- $L_{2,3}$  spectra of BFO/GSO, CoO/BFO/GSO (a) and Ta/Co/BFO/GSO (b) thin films. The insets of (a),(b) show the schematics of the samples. In (b), the spectra are recorded with circular polarized x-rays parallel (red) or antiparallel (blue) with the applied field  $\mu_0 H = 6.5$  T in the OOP direction, at  $T = 4$  K, with the corresponding XMCD at the bottom. To compare the relative simulations of Fe<sup>3+</sup> and Fe<sup>2+</sup> from the atomic multiplet, calculations are also listed at the top. (c) Oxygen  $K$  edge XAS spectra from BFO/GSO and Ta/Co/BFO/GSO at  $T = 4$  K. The spectra for BFO/GSO are roughly divided into Fe  $3d$ , Bi  $6sp$ , and Fe  $4sp$  orbital character regions, while for Co/BFO/GSO, the O  $K$  edge spectra are roughly divided into Co  $3d$  and Co  $4sp$ , and the Bi  $6sp$  peak disappears.

calculations for  $\text{Fe}^{3+}$  and  $\text{Fe}^{2+}$  ions. The  $\text{Fe}^{3+}$  contribution to the XAS and XMCD spectra is relatively small and is not taken into account in the following discussions for the interfacial magnetism.

Figures 4(a) and 4(b) show the  $\text{Fe}^{3+}$  and  $\text{Fe}^{2+}$   $L_{2,3}$  edge XAS and XMCD spectra, respectively. The magnetic field of 6.5 T, which is strong enough to saturate both the Co film at the top and the interface  $\text{Fe}^{2+}$  magnetization, is applied either in-plane or out-of-plane and almost identical XMCD spectra are observed for Co/BFO71 and Co/BFO109. Thus, only the spectra of Co/BFO109 are presented. The XAS spectra of the reference sample CoO/BFO/GSO are also listed for comparison. At the CoO/BFO interface, no formation of  $\text{Fe}^{2+}$  is observed, and the Fe  $L_{2,3}$  edge XMCD intensity is the same as we observe on pure BFO/GSO. While for Co/BFO, the experimental XAS of Fe can be well reproduced with pure  $\text{Fe}^{2+}$  ions without any contributions from  $\text{Fe}^{3+}$  ions. Thus, the  $\text{Fe}^{3+}$  contribution in the experimental XAS and XMCD spectra is small and will not be taken into account in the following discussion. The negative sign of the  $\text{Fe}^{2+}$   $L$  edges XMCD spectra [Fig. 4(b)] indicate that the coupling between the Co and  $\text{Fe}^{2+}$  across the interface is parallel along the field applied during the measurements. The XMCD spectrum suggests that the coupling between the Co film spins and the bulk antiferromagnetic spin lattice of BFO is mediated through the very thin (a few unit cells) alternative magnetic state of  $\text{Fe}^{2+}$  localized at the interface.

Experimental evidence of the Co—O bond can be confirmed in the O  $K$  edge XAS, which directly shows transferred O  $2p$  partial density due to hybridization with the unoccupied orbital states [8,43]. As seen in Kyung-Tae's work [43], for BFO, the spectra are roughly divided into Fe  $3d$ , Bi  $6sp$ , and Fe  $4sp$  orbital character regions. While for Co/BFO/GSO, the O  $K$  edge spectra are roughly divided into Co  $3d$  and Co  $4sp$ , and the Bi  $6sp$  peak disappears since the TEY signal comes from approximately the top few nm of the sample.

Magnetic exchange coupling at the interfaces of Co/BFO is investigated to understand how the magnetic coercivity of the cobalt thin film is affected by the BFO beneath with different domain structures. One can calculate the individual spin moments ( $M_S$ ) and orbital moments ( $M_L$ ) of the cobalt thin film and the interfacial BFO from the XMCD spectra {shown in Figs. 4(a) and 4(b), and Supplemental Material [37] using the sum rules [47,48]}. For the cobalt thin film, given the  $3d$  orbital unoccupied number of  $N_h = 2.49$  [47], the saturated orbital and spin moments at 4 K are  $M_L = 0.26 \mu_B$  and  $M_S = 1.72 \mu_B$ , respectively. The total magnetic moment of the cobalt thin film is  $M = 1.98 \mu_B/\text{Co atom}$ , which is approximately 10% enhanced compared to  $1.70 \mu_B$  in bulk cobalt with a *hcp* structure. For the interfacial BFO ( $\text{Fe}^{2+}$ ,  $N_h = 4$ ) with an external field  $\mu_0 H = 6.5$  T applied at 4 K, both

Co/BFO109 and Co/BFO71 yield the same Fe  $2p$  XMCD spectra. The orbital and spin moments of the interfacial BFO are  $M_L = 0.23 \mu_B$  and  $M_S = 0.88 \mu_B$ , respectively, with the total magnetic moment  $M = 1.11 \mu_B/\text{Fe atom}$  (Supplemental Material [37]). This interfacial magnetism of Co/BFO is commensurate with that observed at the interfaces of  $\text{Co}_{0.4}\text{Fe}_{0.4}\text{B}_{0.2}/\text{BFO}$  ( $1 \pm 0.5 \mu_B/\text{Fe atom}$ ) [12] and of  $\text{La}_{0.7}\text{Sr}_{0.3}\text{MnO}_3/\text{BFO}$  superlattices ( $0.3 \mu_B/\text{Fe atom}$  [23] and  $1.83 \pm 0.16 \mu_B/\text{Fe atom}$  [24]). Note that the theoretical value for the total magnetic moment in bulk iron is  $1.2 \mu_B/\text{Fe atom}$  and the interfacial  $\text{Fe}^{2+}$  shows an approximately 40-fold enhancement compared to that in bulk BFO ( $0.03 \mu_B/\text{Fe atom}$ ).

We discover that the iron sites at the Co/BFO interface are mainly  $\text{Fe}^{2+}$  ions. Both the Fe  $2p$  XMCD spectra of Co/BFO71 and Co/BFO109 samples are dominated by the  $\text{Fe}^{2+}$  spectral features [Fig. 4(b)]. This interfacial  $\text{Fe}^{2+}$  BFO layer is estimated to be about 1–2 atomic layers based on the escape depth of Fe  $2p$  XMCD signals. The formation of  $\text{Fe}^{2+}$  ions at the interface could occur when cobalt atoms are deposited onto the BFO surface and result from the work-function mismatch between cobalt and BFO. Since the signals from the interfacial  $\text{Co}^{2+}$  layer would be shadowed by the 4-nm cobalt film above it, we turn to O  $1s$  XAS to disclose the identity of the interfacial oxide layers. The result [Fig. 4(c)] is consistent with the charge-transfer picture described here.

It is considered that the  $\text{Fe}^{2+}$  of the interface exhibits the antiferromagnetism since the intensity of the XMCD signal of  $\text{Fe}^{2+}$  is reduced to zero with the decreasing applied magnetic field. The model can be treated as the exchange coupling between a ferromagnetic Co layer and the antiferromagnetic layers combined with  $\text{Fe}^{2+}$  and  $\text{Fe}^{3+}$  of the BFO. The exchange interaction can be expressed as

$$E = J_{\text{Co}/\text{Fe}^{2+}} \cdot \mathbf{m}_{\text{Co}} \cdot \mathbf{m}_{\text{Fe}^{2+}} + J_{\text{Fe}^{2+}/\text{Fe}^{3+}} \cdot \mathbf{m}_{\text{Fe}^{2+}} \cdot \mathbf{m}_{\text{Fe}^{3+}}$$

in which  $J_{\text{Co}/\text{Fe}^{2+}}$  and  $J_{\text{Fe}^{2+}/\text{Fe}^{3+}}$  are the exchange integrals of Co/ $\text{Fe}^{2+}$  and  $\text{Fe}^{2+}$ /BFO, respectively.  $\mathbf{m}_{\text{Co}}$ ,  $\mathbf{m}_{\text{Fe}^{2+}}$ , and  $\mathbf{m}_{\text{Fe}^{3+}}$  are the magnetic moments of the Co metal layer,  $\text{Fe}^{2+}$  interface layer, and BFO layer, respectively. The magnetic moment can be expressed in scalar form if only the in-plane projection is considered. Both  $\text{Fe}^{2+}$  and  $\text{Fe}^{3+}$  are in high spin states, and the spin moments are 2 and  $5/2$ , respectively. In both samples, the formation of  $\text{Fe}^{2+}$  and the identical strong XMCD signal are the same, which means not only  $\mathbf{m}_{\text{Fe}^{2+}}$  but also  $J_{\text{Co}/\text{Fe}^{2+}}$  are the same. Therefore, the first term of the formula is equal no matter the domain structure of the BFO layer. And the second term includes the exchange interaction between interfacial  $\text{Fe}^{2+}$  and the BFO film. The exchange integral between the interfacial layer and BFO layer is supposed to be the same in both samples due to the same interaction field. The projection of  $\mathbf{m}_{\text{Fe}^{3+}}$  is determined by the antiferromagnetic moment of the BFO layer. The



XLD results in Fig. 3 indicate that the projection of the spin moment of BFO109 is larger than that of the BFO71 sample due to the compressive strain, which makes the second term larger in the Co/BFO109 sample. Therefore, the exchange interactive energy is larger in the Co/BFO109 sample than that in the Co/BFO71 sample, causing significant enhancement of the coercive field in the Co/BFO109 sample.

It is reported that the exchange field will theoretically achieve 6.5 kOe, nevertheless the value measured in the experiment is only tens of Oe. It is believed this discrepancy originates from the uncompensated spins at the interface [12]. The confirmation of  $\text{Fe}^{2+}$  at the interface makes the interface coupling clear in the Co/BFO system. The formation of  $\text{Fe}^{2+}$  at the interface weakens the coupling between Co and BFO, and as a result, the value of the exchange field is smaller than the theoretical one. All these results indicate that the formation of  $\text{Fe}^{2+}$  plays an important role in studying magnetoelectric coupling and the application of spintronic devices.

#### IV. CONCLUSIONS

To conclude, from the soft x-ray XAS, XLD, and XMCD spectral investigations we show that an alternative magnetic phase  $\text{Fe}^{2+}$  at the Co/BFO interface is induced with a charge transfer from Co to  $\text{Fe}^{3+}$  in BFO. With the relative stronger exchange coupling in Co/BFO109, a stronger enhancement of the coercive field is observed. As reported very recently, the magnetic anisotropy of exchange-coupled  $\text{Co}_{0.9}\text{Fe}_{0.1}$  layers is effectively tuned by using different substrates with the strain to engineer the antiferromagnetic-spin orientation of BFO [49]. Our findings strongly suggest that the interfacial charge transfer plays an important role in tuning the magnetic anisotropy of the upper ferromagnetic layers. We emphasize that the presented interfacial charge transfer not only enables a deeper understanding of the exchange coupling at the metal/BFO interface, but also can trigger alternative ways of preparing and controlling interface properties by means of an electric field.

#### ACKNOWLEDGMENTS

This work is supported by the National Science Foundation of China (Grant No. 51605449) and the Fund for Shanxi 1331 Project Key Subject Construction (Grant No. 1331KSC).

J.W.M., K.C., and T.-C.W. conceived the project and designed the experiments. J.W.M., D.F.C., and Y.Z. prepared all the samples and carried out AFM measurements. K.C. performed all the XLD and XMCD measurements. Z.Q.Z., L.L.W., and G.M. carried out the M-H measurements. J.W.M. and K.C. wrote the manuscript and all authors commented on the manuscript.

- [1] C. Chappert, A. Fert, and F. N. Van Dau, The emergence of spin electronics in data storage, *Nat. Mater.* **6**, 813 (2007).
- [2] L. W. Martin and A. M. Rappe, Thin-film ferroelectric materials and their applications, *Nat. Rev. Mater.* **2**, 16087 (2016).
- [3] G. Catalan and J. F. Scott, Physics and applications of bismuth ferrite, *Adv. Mater.* **21**, 2463 (2009).
- [4] L. W. Martin, Y. H. Chu, and R. Ramesh, Advances in the growth and characterization of magnetic, ferroelectric, and multiferroic oxide thin films, *Mater. Sci. Eng. R-Rep.* **68**, 89 (2010).
- [5] S. Y. Yang, J. Seidel, S. J. Byrnes, P. Shafer, C. H. Yang, M. D. Rossell, P. Yu, Y. H. Chu, J. F. Scott, J. W. III Ager, L. W. Martin, and R. Ramesh, Above-bandgap voltages from ferroelectric photovoltaic devices, *Nat. Nanotechnol.* **5**, 143 (2010).
- [6] D. S. Rana, I. Kawayama, K. Mavani, K. Takahashi, H. Murakami, and M. Tonouchi, Understanding the nature of ultrafast polarization dynamics of ferroelectric memory in the multiferroic  $\text{BiFeO}_3$ , *Adv. Mater.* **21**, 2881 (2009).
- [7] M. Bibes, J. E. Villegas, and A. Barthélemy, Ultrathin oxide films and interfaces for electronics and spintronics, *Adv. Phys.* **60**, 5 (2011).
- [8] P. Yu, J. S. Lee, S. Okamoto, M. D. Rossell, M. Huijben, C. H. Yang, Q. He, J. X. Zhang, S. Y. Yang, M. J. Lee, Q. M. Ramasse, R. Erni, Y. H. Chu, D. A. Arena, C. C. Kao, L. W. Martin, and R. Ramesh, Interface Ferromagnetism and Orbital Reconstruction in  $\text{BiFeO}_3\text{-La}_{0.7}\text{Sr}_{0.3}\text{MnO}_3$  Heterostructures, *Phys. Rev. Lett.* **105**, 027201 (2010).
- [9] P. Fischer, M. Polomska, I. Sosnowska, and M. Szymaniski, Temperature dependence of the crystal and magnetic structures of  $\text{BiFeO}_3$ , *J. Phys. C* **13**, 1931 (1980).
- [10] J. X. Zhu, X. D. Wen, J. T. Haraldsen, M. He, C. Panagopoulos, and E. E. Chia, Induced ferromagnetism at  $\text{BiFeO}_3/\text{YBa}_2\text{Cu}_3\text{O}_7$  interfaces, *Sci. Rep.* **4**, 5368 (2014).
- [11] D. Yi, J. Liu, S. Okamoto, S. Jagannatha, Y. C. Chen, P. Yu, Y. H. Chu, E. Arenholz, and R. Ramesh, Tuning the Competition Between Ferromagnetism and Antiferromagnetism in a Half-Doped Manganite Through Magnetoelectric Coupling, *Phys. Rev. Lett.* **111**, 127601 (2013).
- [12] H. Béa, M. Bibes, F. Ott, B. Dupé, X. H. Zhu, S. Petit, S. Fusil, C. Deranlot, K. Bouzehouane, and A. Barthélemy, Mechanisms of Exchange Bias with Multiferroic  $\text{BiFeO}_3$  Epitaxial Thin Films, *Phys. Rev. Lett.* **100**, 017204 (2008).
- [13] Z. Chen, J. Liu, Y. Qi, D. Chen, S. L. Hsu, A. R. Damodaran, X. He, A. T. N'Diaye, A. Rockett, and L. W. Martin, 180 degrees ferroelectric stripe nanodomains in  $\text{BiFeO}_3$  thin films, *Nano Lett.* **15**, 6506 (2015).
- [14] Q. Zhang, P. Murray, L. You, C. Wan, X. Zhang, W. Li, U. Khan, J. Wang, K. Liu, and X. Han, Magnetic fingerprint of interfacial coupling between CoFe and nanoscale ferroelectric domain walls, *Appl. Phys. Lett.* **109**, 082902 (2016).
- [15] D. Chen, Z. Chen, Q. He, J. D. Clarkson, C. R. Serrao, A. K. Yadav, M. E. Nowakowski, Z. Fan, L. You, X. Gao, D. Zeng, L. Chen, A. Y. Borisevich, S. Salahuddin, J.-M. Liu, and J. Bokor, Interface engineering of domain structures in  $\text{BiFeO}_3$  thin films, *Nano Lett.* **17**, 486 (2017).



- [16] T. J. Regan, H. Ohldag, C. Stamm, F. Nolting, J. Lüning, J. Stöhr, and R. L. White, Chemical effects at metal/oxide interfaces studied by x-ray-absorption spectroscopy, *Phys. Rev. B* **64**, 214422 (2001).
- [17] C. G. Duan, S. S. Jaswal, and E. Y. Tsymbal, Predicted Magnetoelectric Effect in Fe/BaTiO<sub>3</sub> Multilayers: Ferroelectric Control of Magnetism, *Phys. Rev. Lett.* **97**, 047201 (2006).
- [18] S. Valencia, A. Crassous, L. Bocher, V. Garcia, X. Moya, R. O. Cherifi, C. Deranlot, K. Bouzouhane, S. Fusil, A. Zobelli, A. Gloter, N. D. Mathur, A. Gaupp, R. Abrudan, F. Radu, A. Barthélémy, and M. Bibes, Interface-induced room-temperature multiferroicity in BaTiO<sub>3</sub>, *Nat. Mater.* **10**, 753 (2011).
- [19] G. Radaelli, D. Petti, E. Plekhanov, I. Fina, P. Torelli, B. R. Salles, M. Cantoni, C. Rinaldi, D. Gutiérrez, G. Panaccione, M. Varela, S. Picozzi, J. Fontcuberta, and R. Bertacco, Electric control of magnetism at the Fe/BaTiO<sub>3</sub> interface, *Nat. Commun.* **5**, 3034 (2014).
- [20] S. Couet, M. Bisht, M. Trekels, M. Menghini, C. Petermann, M. J. Van Bael, J.-P. Locquet, R. Ruffer, A. Van tomme, and K. Temst, Electric field-induced oxidation of ferromagnetic/ferroelectric interfaces, *Adv. Funct. Mater.* **24**, 71 (2014).
- [21] T. Das and A. V. Balatsky, Engineering three-dimensional topological insulators in Rashba-type spin-orbit coupled heterostructures, *Nat. Commun.* **4**, 1972 (2013).
- [22] S. Singh, J. Xiong, A. P. Chen, M. R. Fitzsimmons, and Q. X. Jia, Field-dependent magnetization of BiFeO<sub>3</sub> in an ultrathin La<sub>0.7</sub>Sr<sub>0.3</sub>MnO<sub>3</sub>/BiFeO<sub>3</sub> superlattice, *Phys. Rev. B* **92**, 224405 (2015).
- [23] S. Singh, J. T. Haraldsen, J. Xiong, E. M. Choi, P. Lu, D. Yi, X. D. Wen, J. Liu, H. Wang, Z. Bi, P. Yu, M. R. Fitzsimmons, J. L. MacManus-Driscoll, R. Ramesh, A. V. Balatsky, J. X. Zhu, and Q. X. Jia, Induced Magnetization in La<sub>0.7</sub>Sr<sub>0.3</sub>MnO<sub>3</sub>/BiFeO<sub>3</sub> Superlattices, *Phys. Rev. Lett.* **113**, 047204 (2014).
- [24] E. J. Guo, J. R. Petrie, M. A. Roldan, Q. Li, R. D. Desautels, T. Charlton, A. Herklotz, J. Nichols, J. van Lierop, J. W. Freeland, S. V. Kalinin, H. N. Lee, and M. R. Fitzsimmons, Spatially resolved large magnetization in ultrathin BiFeO<sub>3</sub>, *Adv. Mater.* **29**, 1700790 (2017).
- [25] Y. Liang, X. Ning, Z. J. Wang, B. He, Y. Bai, X. Zhao, W. Liu, Z. Zhang, and Charge Transfer, Orbital reconstruction and induced magnetic coupling in manganese/BiFeO<sub>3</sub> heterostructures, *J. Phys. Chem. C* **121**, 16810 (2017).
- [26] D. Sando, *et al.*, Crafting the magnonic and spintronic response of BiFeO<sub>3</sub> films by epitaxial strain, *Nat. Mater.* **12**, 641 (2013).
- [27] L. Baldrati, C. Rinaldi, A. Manuzzi, M. Asa, L. Aballe, M. Foerster, N. Biškup, M. Varela, M. Cantoni, and R. Bertacco, Electrical switching of magnetization in the artificial multiferroic CoFeB/BaTiO<sub>3</sub>, *Adv. Electron. Mater.* **2**, 1600085 (2016).
- [28] M. Bibes and A. Barthélémy, Multiferroics: Towards a magnetoelectric memory, *Nat. Mater.* **7**, 425 (2008).
- [29] J. T. Heron, M. Trassin, K. Ashraf, M. Gajek, Q. He, S. Y. Yang, D. E. Nikonov, Y. H. Chu, S. Salahuddin, and R. Ramesh, Electric-Field-Induced Magnetization Reversal in a Ferromagnet-Multiferroic Heterostructure, *Phys. Rev. Lett.* **107**, 217202 (2011).
- [30] J. T. Heron, J. L. Bosse, Q. He, Y. Gao, M. Trassin, L. Ye, J. D. Clarkson, C. Wang, J. Liu, S. Salahuddin, D. C. Ralph, D. G. Schlom, J. Íñiguez, B. D. Huey, and R. Ramesh, Deterministic switching of ferromagnetism at room temperature using an electric field, *Nature* **516**, 370 (2014).
- [31] Y. H. Chu, L. W. Martin, M. B. Holcomb, and R. Ramesh, Controlling magnetism with multiferroics, *Mater. Today* **10**, 16 (2007).
- [32] T. Zhao, A. Scholl, F. Zavaliche, K. Lee, M. Barry, A. Doran, M. P. Cruz, Y. H. Chu, C. Ederer, N. A. Spaldin, R. R. Das, D. M. Kim, S. H. Baek, C. B. Eom, and R. Ramesh, Electrical control of antiferromagnetic domains in multiferroic BiFeO<sub>3</sub> films at room temperature, *Nat. Mater.* **5**, 823 (2006).
- [33] A. Solmaz, M. Huijben, G. Koster, R. Egoavil, N. Gauquelin, G. Van Tendeloo, J. Verbeeck, B. Noheda, and G. Rijnders, Domain selectivity in BiFeO<sub>3</sub> thin films by modified substrate termination, *Adv. Funct. Mater.* **26**, 2882 (2016).
- [34] J. E. Giencke, C. M. Folkman, S.-H. Baek, and C.-B. Eom, Tailoring the domain structure of epitaxial BiFeO<sub>3</sub> thin films, *Curr. Opin. Solid ST. M.* **18**, 39 (2014).
- [35] Y. H. Chu, Q. He, C. H. Yang, P. Yu, L. W. Martin, P. Shafer, and R. Ramesh, Nanoscale control of domain architectures in BiFeO<sub>3</sub> thin films, *Nano Lett.* **9**, 1726 (2009).
- [36] J. Nogues and I. K. Schuller, Exchange bias, *J. Magn. Magn. Mater.* **192**, 203 (1999).
- [37] See Supplemental Material at <http://link.aps.org/supplemental/10.1103/PhysRevApplied.12.044010> for figures showing the magnetic hysteresis of Co/BFO109 at 4 K, the sum rule application for Co, and the sum rule application for Fe<sup>2+</sup>.
- [38] R. Uecker, B. Velickov, D. Klimm, R. Bertram, M. Bernhagen, M. Rabe, M. Albrecht, R. Fornari, and D. G. Schlom, Properties of rare-earth scandate single crystals (Re = Nd-Dy), *J. Cryst. Growth* **310**, 2649 (2008).
- [39] J. T. Heron, D. G. Schlom, and R. Ramesh, Electric field control of magnetism using BiFeO<sub>3</sub>-based heterostructures, *Appl. Phys. Rev.* **1**, 021303 (2014).
- [40] F. Zavaliche, R. R. Das, D. M. Kim, C. B. Eom, S. Y. Yang, P. Shafer, and R. Ramesh, Ferroelectric domain structure in epitaxial BiFeO<sub>3</sub> films, *Appl. Phys. Lett.* **87**, 182912 (2005).
- [41] C. Ederer and N. A. Spaldin, Weak ferromagnetism and magnetoelectric coupling in bismuth ferrite, *Phys. Rev. B* **71**, 060401 (2005).
- [42] C. Y. Kuo, Z. Hu, J. C. Yang, S. C. Liao, Y. L. Huang, R. K. Vasudevan, M. B. Okatan, S. Jesse, S. V. Kalinin, L. Li, H. J. Liu, C. H. Lai, T. W. Pi, S. Agrestini, K. Chen, P. Ohresser, A. Tanaka, L. H. Tjeng, and Y. H. Chu, Single-domain multiferroic BiFeO<sub>3</sub> films, *Nat. Commun.* **7**, 12712 (2016).
- [43] K. T. Ko, M. H. Jung, Q. He, J. H. Lee, C. S. Woo, K. Chu, J. Seidel, B. G. Jeon, Y. S. Oh, K. H. Kim, W. I. Liang, H. J. Chen, Y. H. Chu, Y. H. Jeong, R. Ramesh, J. H. Park, and C. H. Yang, Concurrent transition of ferroelectric and magnetic ordering near room temperature, *Nat. Commun.* **2**, 567 (2011).

- [44] J. C. Yang, *et al.*, Orthorhombic BiFeO<sub>3</sub>, *Phys. Rev. Lett.* **109**, 247606 (2012).
- [45] A. Agbelele, *et al.*, Strain and magnetic field induced spin-structure transitions in multiferroic BiFeO<sub>3</sub>, *Adv. Mater.* **29**, 1602327 (2017).
- [46] E. Stavitski and F. M. F. de Groot, The CTM4XAS program for EELS and XAS spectral shape analysis of transition metal L edges, *Micron* **41**, 687 (2010).
- [47] P. Carra, B. T. Thole, M. Altarelli, and X. Wang, X-ray Circular Dichroism and Local Magnetic Fields, *Phys. Rev. Lett.* **70**, 694 (1993).
- [48] C. Chen, Y. Idzerda, H.-J. Lin, N. Smith, G. Meigs, E. Chaban, G. Ho, E. Pellegrin, and F. Sette, Experimental Confirmation of the X-Ray Magnetic Circular Dichroism Sum Rules for Iron and Cobalt, *Phys. Rev. Lett.* **75**, 152 (1995).
- [49] Z. H. Chen, *et al.*, Complex strain evolution of polar and magnetic order in multiferroic BiFeO<sub>3</sub> thin films, *Nat. Commun.* **9**, 1 (2018).

*Correction:* The author name Yimin Mijiti has been changed to Emin Mijit.